Pharm Res (2013) 30:1147–1160
DOI 10.1007/s11095-012-0950-y

RESEARCH PAPER

Location-Dependent Coronary Artery Diffusive and Convective Mass Transport Properties of a Lipophilic Drug Surrogate Measured Using Nonlinear Microscopy

Joseph T. Keyes • Bruce R. Simon • Jonathan P. Vande Geest

Received: 19 September 2012 / Accepted: 27 November 2012 / Published online: 7 December 2012

ABSTRACT

Purpose Arterial wall mass transport properties dictate local distribution of biomolecules or locally delivered dugs. Knowing how these properties vary between coronary artery locations could provide insight into how therapy efficacy is altered between arterial locations.

Methods We introduced an indocarbocyanine drug surrogate to the lumens of left anterior descending and right coronary (LADC; RC) arteries from pigs with or without a pressure gradient. Interstitial fluorescent intensity was measured on live samples with multiphoton microscopy. We also measured binding to porcine coronary SMCs in monoculture.

Results Diffusive transport constants peaked in the middle sections of the LADC and RC arteries by 2.09 and 2.04 times, respectively, compared to the proximal and distal segments. There was no statistical difference between the average diffusivity value between LADC and RC arteries. The convection coefficients had an upward trend down each artery, with the RC being higher than the LADC by 3.89 times.

Conclusions This study demonstrates that the convective and diffusive transport of lipophilic molecules changes between the LADC and the RC arteries as well as along their length. These results may have important implications in optimizing drug delivery for the treatment of coronary artery disease.

KEY WORDS convection · coronary · DiI · porcine · transport

INTRODUCTION

The approval of drug-eluting stents (DESs) for use in patients by the FDA in 2003 has led to extended research into the drug release, distribution, and reactivity of the stent-tissue complex (1–9). In addition, due to the severity and frequency of coronary artery disease, significant research has been performed on the response of coronary tissues to endocrine and paracrine factors (10,11). Understanding how such molecules transport in the arterial wall can help guide research and therapy. This encompasses, among other factors, understanding how drug release, binding, diffusive transport, and convective transport occur in the body (1,9).

Previously, researchers have performed wet-laboratory and computational studies addressing several of these factors (7,12). For instance, molecular binding studies have provided researchers with a better understanding of the capability of hydrophobic drugs to partition heavily, but move slowly, into the vessel wall (7,12). In addition, studies have been previously performed investigating the importance of the relative physiological forces that determine how transport occurs, and varies, between molecule types (4,12).

A relatively cost-effective alternative to determine drug transport without using the actual pharmaceutical agent is to evaluate the transport of drug-surrogate, or drug-carrying surrogate, molecules. Several different studies have taken this route to better understand arterial molecular transport (13–15). For instance, the use of fluorescently labeled dextran

J. T. Keyes • J. P. Vande Geest
Graduate Interdisciplinary Program in Biomedical Engineering
The University of Arizona, Tucson, Arizona 85721, USA

B. R. Simon • J. P. Vande Geest (✉)
Department of Aerospace and Mechanical Engineering
The University of Arizona PO Box 210119
Tucson, Arizona 85721-0119, USA
e-mail: jpv1@email.arizona.edu

J. P. Vande Geest
Department of Biomedical Engineering, The University of Arizona
Tucson, Arizona 85721, USA

J. P. Vande Geest
BIO5 Institute for Biocollaborative Research
The University of Arizona
Tucson, Arizona 85721, USA

or albumin can determine how transport occurs with hydrophilic compounds or drugs bound to similarly sized albumin. Using fluorescently labeled dextran allows for the study of transport with a large variance in available commercial sizes (3,000–150,000 Da). Correspondingly, researchers have used hydrophobic dyes to see how, for instance, small (<1,000 Da) hydrophobic compounds (like some drugs) move through the arterial wall (15).

While measuring transport can help determine how species will move through the arterial wall, molecules can often act on localized areas by binding to proteins in the wall. This localized binding after diffusing to a particular location has a prominent effect on drug transport modeling because, since drug-eluting stent pharmaceuticals exhibit high partition into the tissue, binding reduces the observed diffusivity, and provides an area for localized accumulation (7). Total tissue partitioning of the drugs occurs through the selective binding to cellular proteins (7,16).

The total transport (convective and diffusive) and binding behavior can be used together to evaluate transport either in laboratory or computational settings (2,4,5). The evaluation of drug transport from stents encompasses a thorough understanding of the stent and tissue environment separately in addition to the coupled affects. Several computational models have looked at these relative influences by either measuring transport properties on their own or by taking previously published values and simulating the interactions computationally (2,7,17,18).

One method of simulating transport is to evaluate the porohyperelastic characteristics (fluid transport, or permeability, and mechanical properties) of the tissue and use the convective transport solution as an input to the total mass transport analysis in a sequential fashion (2,19). Porohyperelastic analysis allows for the prediction of the deformationally dependent interstitial fluid transport properties of the arterial wall. For this type of analysis, experimental input is needed as driven from the governing material laws. For the porohyperelastic analysis of coronary arteries, the permeability from Darcy's law needs to be determined along with the vessel's mechanical properties. For the mass transport portion of the analysis, the diffusivity and convection coupling coefficient need to be determined (19). Performing analysis in this fashion allows analysis of the deformationally dependent properties in the deformed configuration of the arteries.

Previously, we reported on variations in the porohyperelastic properties of de-endothelialized porcine coronary arteries based on location in the coronary arterial tree (20). While that study did show differences in the porohyperelastic properties, to understand the total differences in expected species concentration, the diffusive and convective properties need to be identified for the different arterial regions. There have been some trends indicating that restenosis after DES implantation is different based on location in the coronary vasculature (6,21,22). This could be due to several factors occurring at the different arterial locations such as improper drug delivery, enhanced delivery of proliferation and remodeling biomolecules, or high mechanical stresses that can induce vascular remodeling (23–25). Therefore, the purpose of this manuscript is to report on variations in the mass transport (diffusivity and convection coupling coefficient) between arterial locations with the use of a lipophilic drug surrogate. We also report on the dye-cell binding characteristics compared to certain drugs and the relative time-scales of binding to transport in porcine coronary artery smooth muscle cells.

MATERIALS AND METHODS

Transport Theory

One method to evaluate transport is through the use of coupled diffusive and convective transport termed as porohyperelastic mass transport analysis (19). In this theoretical framework, the relative contributions of diffusivity and convection are coupled through the Eulerian isotropic Fick law to determine the overall transport (Eq. 1) (19):

$$j_i^{cr} = -d^{cc}\frac{\partial c}{\partial x_i} - b^{cf}ck^{ff}\frac{\partial p^f}{\partial x_i}, \tag{1}$$

where j_i^{cr} is the total molecule flux [mol/m^2_s], c is the concentration [mol/m^3], x_i is the deformed position coordinate [m], b^{cf} is the effective convection coupling coefficient [unitless], d^{cc} is the effective diffusivity [m^2/s], k^{ff} is the permeability [m^4/N_s], and p^f is the interstitial pore fluid pressure [Pa]. Note the second term on the right hand side, where the influence from pore fluid pressure occurs, and the first term where the influence from the chemical potential occurs. The use of $b^{cf}ck^{ff}dp^f/dx_i$ couples the deformation to the total species flux through a series of previously demonstrated ABAQUS/Fortran subroutines (19). These routines allow for the simulation of convective-diffusive transport in the Eulerian domain (on the deformed geometry) for detailed finite element analysis of mass transport.

Sample Preparation

Testing occurred according to approved protocols with the University of Arizona Institutional Animal Care and Use Committee. Porcine hearts (n=5) were obtained from the University of Arizona Food Products and Safety Laboratory within 30 min of sacrifice from barrow pigs weighing roughly 287 ± 34 lb (live weight) at ages of 5–7 months. Hearts were measured across their major axes: apex to coronary

ostia (ACO), transverse at the auricles (TAA), and sagittal at the ostial level (SOL) (26,27). Hearts with dimensions outside of the mean (ACO = 113, TAA = 80, SOL = 69 mm) by more than 10% were not used. Dimensions were used instead of the weight because residual blood in the heart chambers and vessels was not consistent between hearts. The LADC and RC arteries were located and marked at several locations along the length with a cyanoacrylate/ceramic powder mix. Suture lines were laid on the arteries between marker sets and cut and measured before and after removal of the arteries from the myocardium. The ratio of the lengths of the suture lines before and after removing the arteries provided the *in situ* prestretch measurements ($\lambda_{z\text{-}in\ situ}$). Removed arteries were cleaned of any extraneous tissue (fat, muscle) and most of the adventitia, and then split into thirds down the axial length (proximal, middle, and distal; 16.2 ± 5.2 mm in length). Arteries were mechanically de-endothelialized by soft rubbing with non-serrated forceps to ensure transport was measured through the arterial wall in a situation where the endothelium is damaged (e.g., stenting scenarios) (28,29). Denuding was confirmed with trypan blue after testing (data not shown). Arteries were placed into 6-well plates, and the entire segments cultured for 24 h with standard porcine smooth muscle cell media (DMEM with 10% FBS, 1.2% penicillin/streptomycin, 0.9%l-glutamine, 0.1% fungizone) (Cell Applications, Inc; San Diego, CA). After 24 h, the arteries were removed from the well plates, cannulated with silicone tubes then mounted in the testing fixtures. Cannulation was done ensuring the vessel segments did not leak from the cannulation point or any branching vessels. Testing fixtures were filled with CO_2-independent media with the same supplements as the DMEM (Invitrogen; Carlsbad, CA). One adjacent section, 1–2 mm in length, was fixed in 2% paraformaldehyde, and the opposing adjacent section was placed in an SMC isolation solution (294 U/ml collagenase, 5 U/ml elastase, 2 mg/ml BSA, and 1 mg/ml soybean trypsin inhibitor) (Invitrogen; Carlsbad, CA).

Transport Testing

Figure 1 shows the testing fixtures. The bioreactor is a polycarbonate container with a silicone gasket seal, with holes used for either cycling cell media or the drug surrogate. The drug surrogate chosen was the lipophilic indocarbocyanine dye 1,1′-Dioctadecyl-3,3,3′,3′-tetramethylindocarbocyanine perchlorate (synonym: DiI) (Invitrogen; Carlsbad, CA). Like the drugs used on the most frequently used drug-eluting stents (sirolimus and its derivatives, and paclitaxel) the dye is hydrophobic, soluble in ethanol and DMSO, with a similar molecular weight (966 Da for zotarolimus, 854 Da for paclitaxel, 933 Da for DiI) (16,30,31). The logP values indicate that DiI partitions more preferentially into octanol than the drugs, although the drugs do still have logP values greater than one (4.7 for zotarolimus, 12.0 for DiI) (32–38). Concerning solubility, sirolimus maintains solubility roughly 10 mg/ml in DMSO (39), and DiI solubilizes at 18.9 mg/ml from non-agitated solubilization experiments conducted at our laboratory. Solubilization saturation was deemed to occur when powder was added with visible particulates left after 1 h. In addition to these metrics, the free-solution diffusivities are similar in magnitude (3.89e-12 m^2/s for sirolimus (40); 6.89e-12 m^2/s for the dye as measured in our laboratory). These diffusivities are important because they give an indication of the Stokes-Einstein radius (r), which is an indication of the ability to diffuse. This is calculated with $r=kT/(6\pi\mu D)$, where k is the Boltzmann constant, T is the absolute temperature, μ is the viscosity, and D is the free (in-solution) diffusivity (41). Substituting the free diffusivities of paclitaxel, sirolimus, and DiI results in Stokes-Einstein radii of similar magnitude (11.2 nm for paxlitaxel, 26 nm for sirolimus, and 58 nm for DiI) (8,16,40). Sirolimus and its derivatives act by binding to FK506-binding protein, forming a trimeric complex with the mammalian target of rapamycin protein kinase leading to the arrest of the cell cycle progression (42). Paclitaxel is a microtubule destabilizer. While the drug surrogate does not act on the cell to inhibit growth, DiI does still preferentially bind to the cell. DiI binds to the membrane then diffuses laterally to completely stain the membrane (30). Cells labeled with DiI will still maintain viability and can be tracked over time.

Arteries were mounted inline at their measured *in situ* axial prestretch with either a dye injection syringe pump or pressure head, and CO_2-independent media was continuously cycled over the top and inside of the arteries for 2 h at 0.1 mm^3/s. After this period, the pumps were turned off and the dye was injected at a concentration of 0.119 mg/ml. Dye was prepared similar to Li *et al.* (43); however, PBS was replaced with the CO_2-independent cell media. For diffusivity testing the dye was injected at a slow rate (0.1 µl/h) to ensure the artery was not pressurized during dye injection into the lumen. Pressure was monitored with a gage to ensure luminal pressure did not increase beyond 5 mmHg. For the convection coefficient test, the dye tube was connected to a pressure head filled with dye at 100 mmHg, instead of the slow-rate infusion pump. *In vivo*, the pressure-driven scenario is most applicable. However, both diffusivity and convection coefficient were measured independently in order to provide the constants needed to computationally model species transport, as governed by Eq. 1. In addition, this provides an indication as to the relative amount of convective or diffusive dominance of the artery with the surrogate.

To measure dye transport through the thickness of the vessels at different time points the bioreactor, and all fluid and pressure components, were placed under an upright multiphoton microscope. The bioreactor was placed on a heated stage to maintain a bath temperature of 37°C. A

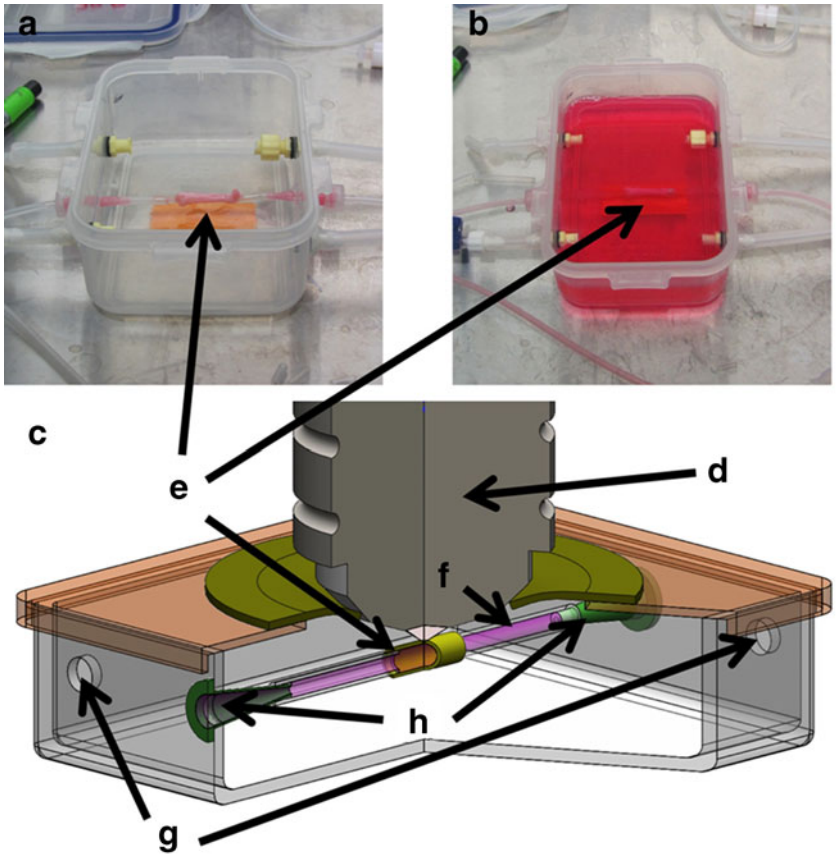

Fig. 1 Mass transport testing fixture. (**a**) shows the vessel (**e**) in the fixture before filling with cell media. (**b**) is after filling with media. (**c**) is a schematic of the fixture with a cutaway showing the dye in the inlet tube (**f**), and the microscope objective (**d**). (**h**) and (**g**) are the dye and media flow connectors, respectively.

water-dip objective (20X) was placed into 70% ethanol for 30 min and then dried in a UV hood before insertion through a hole in a silicone cover on the bioreactor chamber (see Fig. 1). Plugging the hole in the silicone sheet allowed the system to maintain sterility during the imaging sequences. Scans were made through the thickness of the vessel collecting collagen, elastin, and DiI fluorescence. Imaging was done similar to previous studies to collect extracellular matrix (ECM) components (collagen and elastin) at 780 nm excitation with 28 mW power with linear scaling to 39 mW (44). After this scan was completed, the configuration was changed to excite at 700 nm with 34 mW power with linear scaling to 61 mW to collect dye fluorescence. This was performed at times of 4, 8, 12, 26, and 50 h for the diffusivity tests, and 4, 8, 12, 16, and 24 h for the convection coefficient tests. After each imaging session, the dye was imaged at concentrations of 0.30, 0.10, 0.05, 0.01, 0.005, and 0.001 mg/ml with the same linear scaling of power. This provided a relationship between power, intensity, and concentration; it also provided an indication of the uniformity of fluorescence over the field of view (to be corrected later). The detection limit for the highest power used during testing occurred at 0.2 ppm. This was deemed as the point where the increase in fluorescent intensity was higher than the highest value of noise. At the end of the full time-course of the test the samples were fully submerged in 0.119 mg/ml DiI solution for 24 h. A final multiphoton scan of the saturated sample was then performed. This scan provided an indication of attenuation of the interstitial intensity through the sample.

Image Processing

Images were processed as shown in Fig. 2. The background was subtracted from the original dye scan and then convoluted with a Gaussian surface to smooth any noise. The smoothed image was divided by the maximum pixel value and then the reciprocal taken resulting in a matrix (the non-uniformity correction matrix: NUCM) that can be multiplied by the corresponding tissue image at that particular z-depth to shift all pixels to the maximum to even out the intensity over the field of view. This process corrects noise, vignetting, and misalignment. Precision as measured by the full width at half maximum of the corrected image histogram was 3.0 ± 0.1 intensity units (17 ± 3.8 when uncorrected). Accuracy in these images had up to 2.6% variance when comparing intensity to concentration in solution. To determine the interstitial concentrations, c, the ECM and cells in the dye image need to be eliminated. This occurs by taking the composite ECM image (collagen plus elastin) for

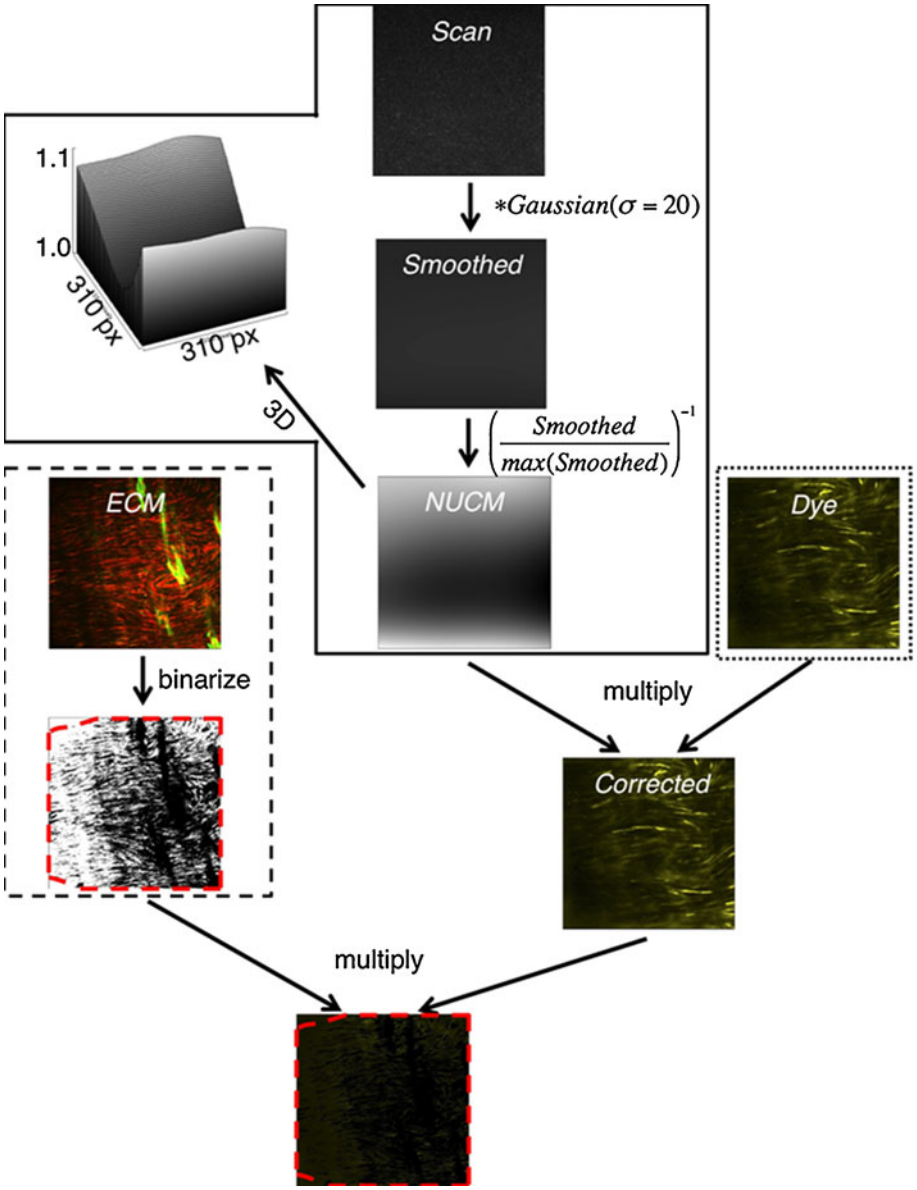

Fig. 2 Image preprocessing sequence. The *solid outlined area* is the area to correct for nonuniformity in the field-of-view, the *dashed area* is the pre-processing to account for non-void (extracellular matrix) space, and the *dotted image* is the raw dye image. In the solid area a scan is made of the dye at several depths with several different powers. A Gaussian smoothing filter is applied then a non-uniformity correction matrix (NUCM) developed that shifts values lower than the maximum to the maximum via a multiplicative operation. The NUCM is multiplied by the raw dye image to even illumination over the field-of-view. The ECM (SHG and autofluorescence images) are binarized where zeros correspond with ECM signal. This image is multiplied by the corrected dye image to isolate interstitial and cell space. The cells are subtracted by eliminating high-intensity pixels (~20 times larger than the interstitial space).

the slice corresponding to the dye, binarizing it after thresholding with a maximum entropy routine (where zeros correspond with tissue), and multiplying it by the corrected dye image. The ECM image also provides an indication of areas with tissue to evaluate the interstitial space (red outline). This outline was created by examining the furthest extent of ECM (zero) signal and connecting boundary tissue locations with straight lines. Cells were subtracted out by eliminating bright spots through outlier subtraction since cells appear roughly ten times brighter than any interstitial space. This is an inherent property of the dye since dye molecules accumulating in the membranes exhibit higher fluorescence than free-dye. Other SMCs that did not exhibit binding were captured as bright non-fibrous bands in the autofluorescence channel, as had been shown previously (45), and were subtracted out.

This process was done for each image slice for all image stacks. After initial image processing, the images were corrected by an attenuation function. The Beer-Lambert law describes optical attenuation (Eq. 2) (46):

$$\alpha z = -log\left(\frac{I}{I_o}\right), \tag{2}$$

where α is the attenuation coefficient [m^{-1}], z is the coordinate through the radius [m], I is the current interstitial intensity [unitless], and I_o is the interstitial intensity at the material interface of the bath to tissue [unitless]. The average interstitial intensity (taken from the pixel average in the interstitial space for a given slice) was corrected by the percent reduction in intensity for each point through the depth based on the particular attenuation function corresponding to the individual sample.

Fig. 3a shows a representative attenuation plot with a fit from Eq. 2. The attenuation coefficient varied by a maximum of 3.3% for any given arterial region, an indication of the accuracy of the correction.

The intensity was related through intensity *versus* concentration calibration curves while matching the powers delivered from the laser for specific slices through the artery wall. Fig. 3b shows a representative calibration surface. Since calibration was done for each image stack, the repeatability doubled from the in-solution accuracy measurements. The ratio of the intensity in the arterial wall to the intensity in solution provides an indication of the partitioning of the solution to interstitial space. Intensities in the calibration curve were corrected by the partition coefficients of the particular vessel segments and the 3-dimensional calibration function relations to result in concentrations in the units of mol/m^3, where m^3 the interstitial volume.

Transport Data Fitting

At this step, a series of radius *versus* average (over the scanned field of view) concentration points existed for the different arteries at the different time points. To relate these to Eq. 1, finite element models were developed of each arterial section in ABAQUS 6.9. The finite element solving scheme has been demonstrated previously and uses a sequential approach to simulate porohyperelastic mass transport (19).

First, an Eulerian porohyperelastic analysis was run using 1/10 circumferential symmetry with elements having a cylindrical coordinate system (r, θ, z) to apply material and boundary conditions. Diameters and thicknesses were taken from histology (Table I) (20), and modeled to be as long axially as it was thick. Each model had ten elements across each direction. Elemental density was determined by examining mass flux with the transport models until the relative fluid velocity, stress, and strain was unchanged to 0.1%. The porohyperelastic models were fixed on one end in z, and the other end stretched to the *in situ* axial stretch. The circumferential edges were fixed in θ as a symmetry condition. To determine d^{fc}, the only further boundary condition was a pore fluid pressure of zero on the entire model. The porohyperelastic states (deformation gradient tensor-F_{ij}, $\mathcal{J} = \det(F_{ij})$, porosity = n, and p^f) were used as input to the mass transport analysis (19). ABAQUS simulates Lagrangian mass transport with concentrations in units of mass per total volume (solid plus fluid). The concentrations from the ABAQUS were converted via the relationship in Eq. 3:

$$\hat{c} = M^c \mathcal{J} n c, \tag{3}$$

where $\hat{c}$ is the mass concentration [kg/m^3], and M^c is the molecular mass [kg/mol]. Since ABAQUS solves for the solution variable, activity (concentration normalized by the solubility of the species in the transporting media), the solubility was imported in ABAQUS as a field variable via Eq. 4:

$$\hat{s} = (M^c/\gamma^c)\mathcal{J} n, \tag{4}$$

where $\hat{s}$ is the solubility of the species in the porous media [kg/m^3], and γ^c is the reciprocal of the molar interstitial solubility [m^3/mol]. After running an analysis and converting the concentrations, the concentration *versus* radius curve was compared between the ABAQUS results and the experimental observations. A Matlab-Fortran-ABAQUS optimization routine was used to fit for different values of d^{fc} to match the experimental to computational concentration profiles (20,47).

Table I Arterial Dimensions (Mean ± Standard Deviation)

	Inner radius (mm)	Thickness (mm)
LP	1.97 ± 0.13	0.26 ± 0.02
LM	1.18 ± 0.14	0.23 ± 0.03
LD	1.03 ± 0.09	0.19 ± 0.05
RP	1.97 ± 0.15	0.29 ± 0.08
RM	1.75 ± 0.36	0.30 ± 0.05
RD	1.91 ± 0.16	0.28 ± 0.02

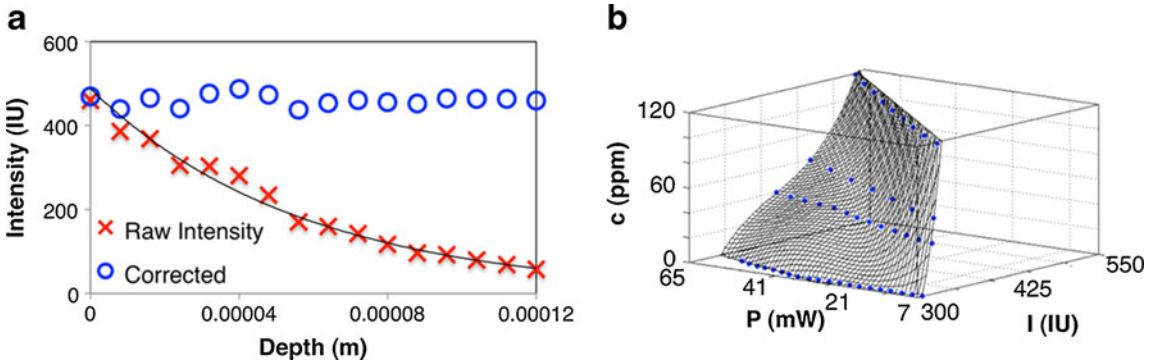

Fig. 3 Attenuation correction function determined by scanning a sample that was allowed to fully saturate in the dye for 24 h. Interstitial intensity values from the experiment are corrected by adding the percent attenuation determined from the fit.

The resulting Eulerian d^{cc} was converted to the Lagrangian diffusivity ($\widehat{\widetilde{D}}_{ij}$) via Eq. 5 (19):

$$\widehat{\widetilde{D}}_{ij} = d^{cc}_{ij} H_{ij}/n, \tag{5}$$

where $\widehat{\widetilde{D}}_{ij}$ is the Lagrangian diffusivity [m^2/s], and H_{ij} is the Finger's strain tensor [unitless]. This was done for each sample that was tested for diffusivity.

To fit for b^{cf}, a similar Matlab-Fortran-ABAQUS routine was utilized. The porohyperelastic model for fitting for the convection coefficient was fixed in displacement the same way as was done for diffusivity fitting. A mechanical and pore fluid pressure condition corresponding to the test pressure was imposed on the inner surface of the vessel (100 mmHg), and a zero pore fluid pressure condition imposed on the adventitial surface. This model was stretched then run to consolidation, and the porohyperelastic characteristics (pore fluid pressure field, pressure stress factor, permeability, mechanical state) exported to the mass transport model. The same optimization routine was run, this time using the average d^{cc} for each arterial section, and optimizing for different values of b^{cf} until the ABAQUS result matched the experimental data using the sum of the square of the residuals.

Cellular Binding

While transport fitting determines how molecules move through the arterial wall, binding characteristics govern how efficiently the molecules bind to their targets. While we examined transport in the different arterial sections, we assumed that cells behave similarly between sections, with the only potential variation in total tissue partition occurring due to cellular density. Potential binding points (due to cellular density), can influence how transport changes between sections as demonstrated by Goriely *et al.* (12). Therefore, this information is necessary to properly model tissue concentrations of species. Histology sections were stained with H&E and counted to determine if any density variations exist between arterial regions and through the thickness (as binned into thirds through the radius).

To examine the dye-to-drug similarity, the bulk partition was determined by fully saturating segments with dye. The segments were introduced to sequential elution baths consisting of trypsin/EDTA (0.25%) for the first two baths, Triton-X and PBS for one bath, and PBS for all remaining baths until no fluorescence was able to be observed in the tissue. The concentrations of the eluted volumes indicate the original tissue concentration (14). The ratio of the tissue concentration to original cultured dye concentration indicated the tissue-binding coefficient. A section normal to the segment's axis was embedded in freeze media, frozen with liquid nitrogen, and cut and imaged with epifluorescence microscopy for cell and non-cell intensity through the radius (for comparison to sirolimus and paclitaxel).

To determine the temporal characteristics of binding, isolated smooth muscle cells were seeded, and at fourth passage introduced to the dye/media solutions in Table II. At time points of 15, 30, 60, 180, and 1,440 min the dye was removed and washed five times with PBS and replaced with media to image the dye intensity in the cells. Media was replaced with the dye between each imaging state. After the final images were taken, dye was removed and replaced with media. Trypsin/EDTA (0.25%) was added and the petri dish gently rocked until all cells were detached. FBS was added, and the solution aspirated and rinsed five times with PBS. Lysis buffer (1% Triton-X with TRIS buffer) was added to the solution, and the solution was sonicated five times (60 s intervals with 30 s pauses). No cells were visible after this process. This solution was imaged to determine the original cellular intensity (prior to membrane disruption). The cell concentration was taken as the concentration of this solution multiplied by the volume of the bath, and then divided by the volume of all the cells. The volume of the cells was taken as the spread of the adhered cells multiplied by the average height as measured from a z-scan using multiphoton microscopy. This provided an indication of the partition of the native dye to the bound concentration in the cell since the dish was washed of all free dye prior to membrane disruption. Binding was fit in ABAQUS using the film coefficient in mass transport (Eq. 6):

$$j_{bind} = -h(c)(b - b_{max}), \tag{6}$$

where $h(c)$ is the film coefficient [m/s] (also termed the binding coefficient; this incorporates cellular area and the surrounding concentration), b_{max} is the maximum bound concentration [mol/m^3] (from the lysis step), and j_{bind} is the concentration flux [mol/m^2_s]. Fitting was accomplished with an optimization routine similar to that run to fit for the transport constants. In this model a planar array of elements was created and a single node selected to represent a cell. The concentration of all nodes outside of the cell were assigned concentrations corresponding to the different tests and different h values optimized for until the temporal concentration at the cell location matched between ABAQUS and the experimental result. Higher values indicate that the cell will reach saturation faster (as indicated by Eq. 6). A table lookup was reported since higher surrounding concentrations will cause the cell to

Table II Mean Binding Coefficients (With Standard Deviation)

$\widehat{c}$ (kg/m^3)	h (m/s)
6.0E-05 (4.1e-6)	1.2E-05 (8.2e-7)
1.2E-04 (3.0e-6)	1.9E-05 (4.8e-7)
2.3E-04 (4.4e-6)	2.8E-05 (5.4e-7)
1.5E-03 (1.2e-5)	5.0E-05 (4.0e-7)

uptake dye at a faster rate. Quantitatively, this value, when multiplied by the maximum bound concentration minus the current bound concentration provides a concentration flux at the local site. This can be multiplied by the exposed cellular area to indicate the mass per unit time binding to the cells.

Statistical Methods

All values are reported as means ± standard deviations. Comparisons were made between groups (LADC *versus* RC; proximal *versus* middle *versus* distal) using two-way ANOVA with a Bonferroni adjustment to determine significance between group-pairs.

RESULTS

Figure 4 shows a representative set of images from diffusion testing. The collagen and elastin is shown as red and green, respectively. Dye is shown in blue. The brighter blue strips are smooth muscle cells. Note that the cells are not visible towards the adventitia due to lower surrounding concentrations, and therefore lower potential for binding. A representative set of data points and the fit from the transport optimization routine are shown in Fig. 5 for a RC middle section. The curves have the characteristic trends for both diffusive and convective-diffusive transport with convection driving the solution to steady-state in a shorter timescale than diffusion alone.

Diffusivity (Fig. 6—Top) showed differences between arterial regions (two-way ANOVA $p<0.05$); however between the LADC and RC there was no statistical

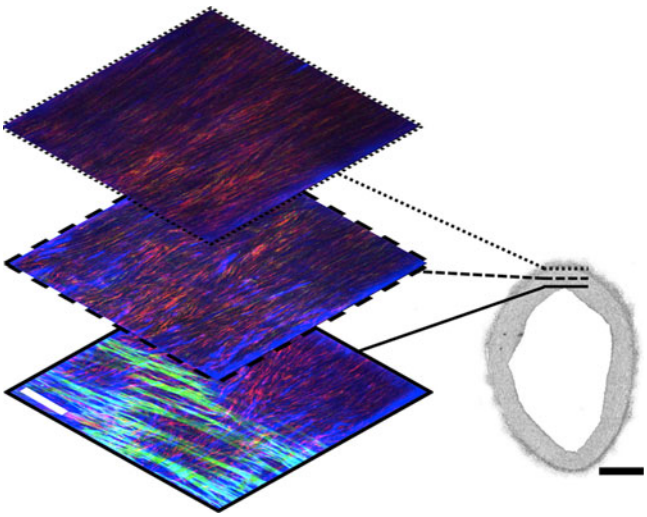

Fig. 4 Representative images through a LADC distal segment. The bottom-most image is towards the lumen. The histology section to the right shows an H&E stain with paraffin embed. Scale on multiphoton images = 50 μm. Scale on histology is 250 μm. In the multiphoton images, *red* is collagen, *green* is elastin, and *blue* is DiI fluorescence.

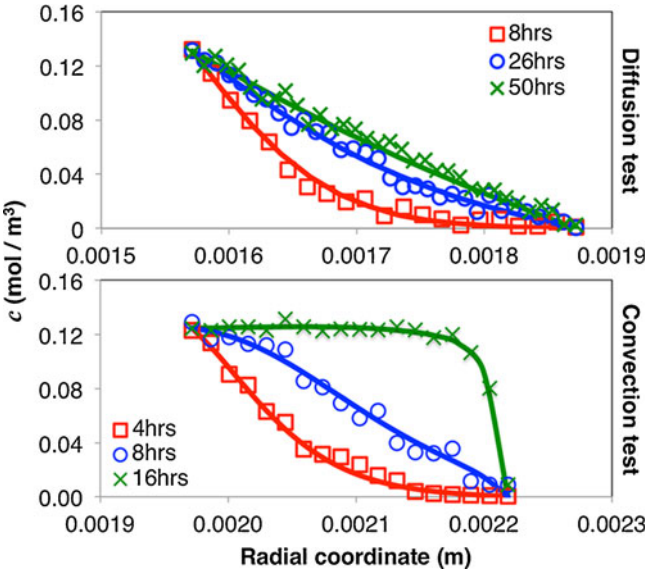

Fig. 5 Representative datasets (*points*) and fits (*solid lines*) from ABAQUS for RC proximal segments for the diffusion and convection coefficient tests. The concentration is the molar concentration (*mol/m*^{3} interstitial volume) in the interstitial voids.

significance. Each vessel had a similar trend down the lengths with middle regions having higher diffusivity than the neighboring proximal and distal regions ($p<0.05$). This comparison between the vessels at the same regions (e.g., comparing proximal to proximal) showed no statistical difference.

The Eulerian convection coefficient (Fig. 6—Bottom) displayed differences between regions; however it showed different trends than the diffusivity (two-way ANOVA $p<0.05$) with a statistical significance between the LADC and RC arteries. The value for b^{cf} was higher in the distal regions than the proximal and middle regions. The proximal and middle regions were not statistically different. There was an order of magnitude difference when moving from the smallest value (LADC proximal), to the largest (RC distal).

The cellular density was unchanged between regions and through the thicknesses (data not shown). Histological sections presented smooth muscle cells as separated bands with bundles of collagen and elastin separating the layers. When investigating cell binding in monoculture, the data fit Eq. 6 with $R^2>0.95$ for all tests (Table II). Figure 7 shows an example of binding with the representative fit. Binding occurred at focal points in the cell membrane and then diffused within the membrane while more binding occurred until a saturation point. The timescale to cellular saturation was 10 and 4 times quicker than the steady state times for diffusive and convective transport, respectively.

A cross section of a saturated sample indicated a relatively flat distribution of both cellular and interstitial dye through the thicknesses (Fig. 8). Cellular concentration through the thickness had a more evenly distributed intensity than the

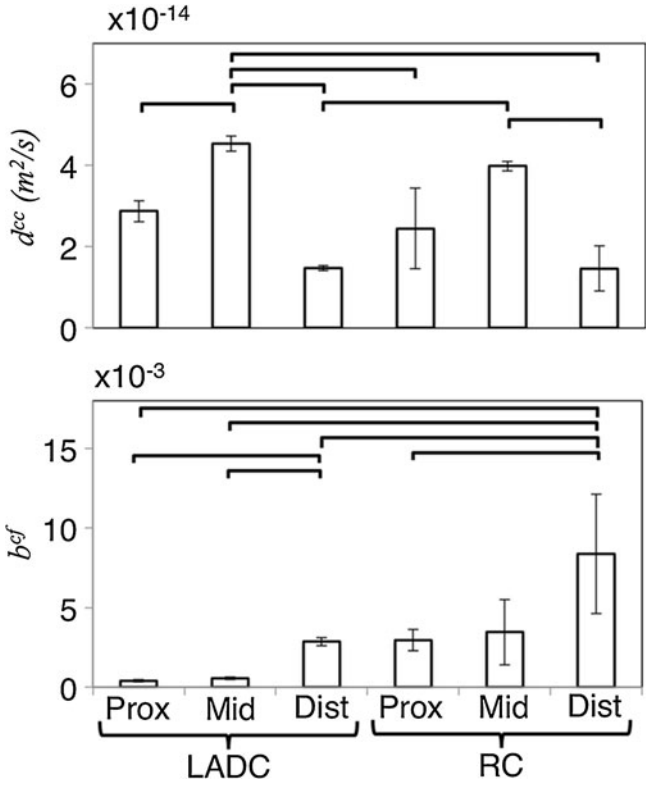

Fig. 6 Diffusion and convection coefficient values for the different arterial segments. *Bars* indicate pairwise significance ($p < 0.05$).

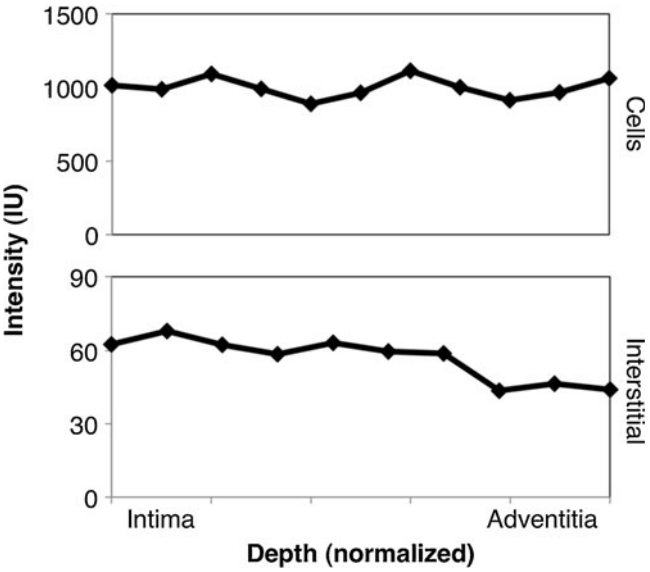

Fig. 8 Cross section (normal to vessel axis) intensity of a saturated sample indicating interstitial and cellular binding distribution.

interstitium. Moving from the media to adventitia the intensity dropped by 31% in the interstitium. Total tissue binding coefficients were 55 ± 10 with no statistical differences between arterial sections.

DISCUSSION

We showed in this study how mass transport characteristics vary between coronary artery regions. We showed this

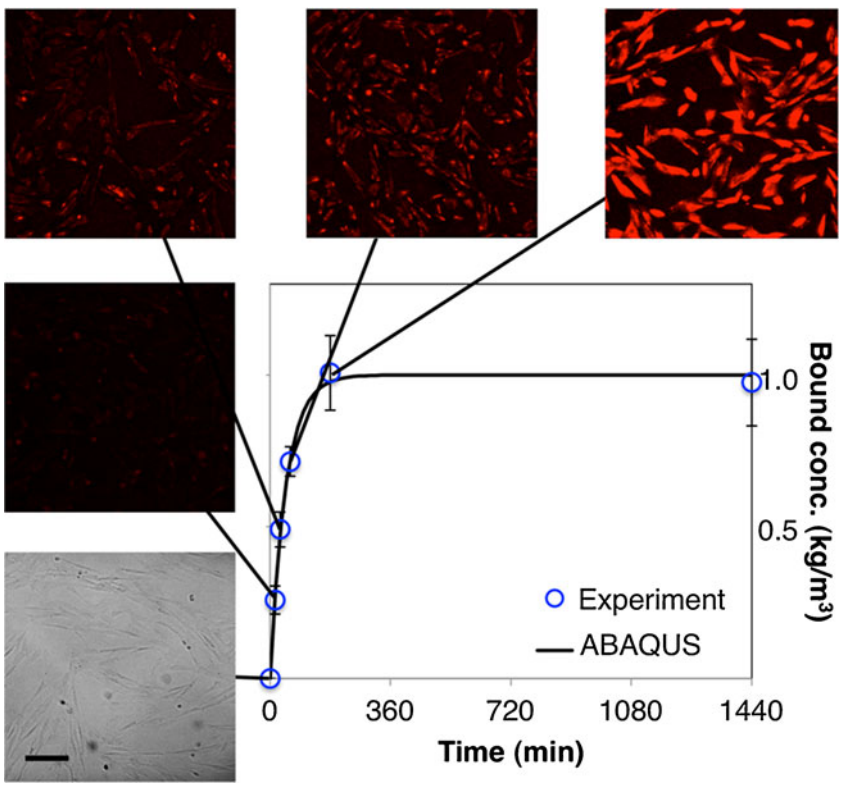

Fig. 7 Representative images of the porcine SMCs from monoculture binding experiments. The scale is 50 μm.

through the use of an off-the-shelf lipophilic dye with similarities to some currently used pharmaceuticals on drug-eluting stents. Observing concentration *en face* with nonlinear microscopy allowed for the evaluation of how concentration changes in saturated samples over time on the same *living* sample. Diffusive transport peaked in the middle regions of both the LADC and RC arteries, whereas convective-diffusive constants increased down the length of each artery. Cell binding occurred a higher rate than transport with a high partition into the cell membrane.

The study of mass transport is a frequently studied topic due to its broad physiological relevance. For instance, it has been shown previously that the transport of hydrophobic drugs is significantly different than that for hydrophilic drugs, with generally better retention and slower transport velocities when using hydrophobic compounds (4). We saw similar behavior to these previous studies with the drug surrogate we used. However, previous studies have not reported on differences along the entire length of a coronary artery or between coronary arteries.

A frequently studied fluorescent surrogate is fluorescein and fluorescein-related molecules, such as fluorescein isothiacyanate. These molecules transport significantly faster than what was observed in our study: 2–4 orders of magnitude higher (3). We expected these differences because pilot studies in our laboratory showed diffusion of FITC-dextran into agarose gels (5%) had diffusivities five orders of magnitude higher than DiI in agarose. In agarose, we believe these differences can be attributed to the solubilized solution. The dye in the indocarbocyanine-applied solution is in a relatively stable (low Gibbs free energy) mixture. This solution is specific to maintain solubility, and therefore initial transport into gel would be more thermodynamically unstable. With highly water-soluble molecules, the stability is more equivalent between the water in the gel and the water surrounding the hydrophilic compounds. In the tissue, this effect influences the slower transport along with the effect of binding since it has been demonstrated previously that binding lowers the effective diffusivity of the porous network (12). Some other transported molecules have slower diffusivities due to these effects, along with the added effect of hydrophobic interactions with globular proteins. These interactions cause increased viscous dissipation of kinetic energy, thereby allowing higher bulk partition with slower diffusion (8).

The effective diffusivity of hydrophobic drugs that are currently used on stents showed that our drug surrogate was on the same order of magnitude to that of paclitaxel and sirolimus (5,48). Considering the total tissue partition was higher with the dye (7), the slower diffusion was expected since binding diminishes effective diffusivities (12).

The observed diffusion is a function of several microscopic factors. For instance, if microstructural components (e.g., exposed repulsion sites in microstructure) are different between regions the solvent shell and dispersion reactions could be influencing how transport varies between regions (49). This could be examined in a computational manner in which charge densities in the ECM are changed and the movement of molecules observed (49). Assuming ECM and cellular molecular components are the same between regions, the observations could be a function of the microstructure. Previous work indicated that the void ratios through the thicknesses were relatively consistent between regions (20). However, the void ratio of the intimal layer changed between regions with the lowest intimal void ratio occurring at the intimal layer. The effective diffusivity in a porous medium can be thought of as an interconnected network of pores whose length scale dictates Knudsen-type diffusion through individual path lengths (50–52). The effective diffusivity takes the form of $D_{eff} = 6aD_o/\pi R$, where a is the radius of the interconnected spheres, R is the radius of the well spheres, and D_o is the solution diffusivity. The smaller voids observed in the middle regions could potentially be thought of as the well pores therefore (from the above equation) increasing the D_{eff} with the assumption that connecting spheres are similar in size. Regarding the changes in b^{of}, this could be a function of the mechanical properties and observations in the void ratio. The RC arteries were more compliant, therefore more deformable than LADC arteries given the same pressure (20). As the porous material deform, paths for transport could begin to merge as has been shown previously with diffusion of electrons through micropores (53). Upon radial compression (as is what happens during intraluminal pressurization), the voids in the transverse direction could be made larger with added connectivity as the voids in the intima enlarge. Therefore, upon pressurization the more compliant an artery is (as the RC arteries are), the more the voids will enlarge in the transverse direction, therefore providing more free path lengths and increasing convective transfer (19).

Additional studies have investigated the effect of the endothelium on transport. We removed the endothelium from vessels tested in our study to capture how transport occurs in situations of percutaneous coronary intervention. In a previous study there was a 50% increase in diffusivity with the removal of the endothelium (48), albeit this previous study was performed with the hydrophilic compound, heparin. This could change dramatically with the use of carbocyanine dyes since the dye would bind to the endothelial cells causing a far lower effective diffusivity. Given that transport occurs in stented vessels in local areas of endothelial denudation via injury (the stent strut locations) (54), culturing smooth muscle cells in a vessel without an endothelium is most appropriate. A future goal of this work is investigating how the properties we report here could be modified in a scenario where the endothelial and smooth muscle cells are kept alive in co-culture, and then a stent implanted. This would allow researchers to explain how between-strut endothelial cells (since strut locations locally denude the primary transport areas) influence transport.

The observed behavior of the increases in b^{σ} along the arterial length seemed to counteract the trends observed in permeability (20). The downward trends in permeability indicate reduced time-of-flight and therefore reduced binding affinity, which affects transport properties. These results indicate that distal transport of molecules in the coronary arterial tree is more heavily influenced by convection.

While the selected dye does transport and bind with similar magnitudes to the most frequently currently used drugs on drug-eluting stents, the dye has some noticeable differences. While they both target cellular components, thus mimicking the general area of binding in the arterial wall, the relative concentrations of the targeted binding proteins are different, with phospholipid concentrations existing at 4–20 times higher than tubulin or FKBP12 (55,56). This could potentially be responsible for differences seen in the total tissue partition observed with the dye *versus* the drugs along with the larger Stokes-Einstein radius of the molecule (16). The tissue binding coefficients were roughly 20–40% higher for the dye compared to sirolimus and paclitaxel. The radial distribution of the dye most closely matched that seen with sirolimus (even distribution instead of adventitial accumulation) (7). This indicated the dye is a good surrogate in this regard. In addition, the dye exhibited a high partition into octanol and solubility into DMSO. Based off of these observations and other tests regarding transport of drugs into arteries we would expect higher diffusivities in all sections if this study were done with DESs drugs given the binding effects. More available binding sites reduces the diffusivity because the observed effective concentration gradient is reduced. Assuming that FKBP12 sites are homogenously distributed through the thickness and length, we would not expect differences in the observed trends in interstitial transport because the free diffusivity and Stokes Einstein radii are similar between the drug and surrogate.

Reporting the effective diffusivity provides researchers with an indication of how this particular drug surrogate will move through the different tested vessel regions. However, this diffusivity is not just how the native molecules would move through the ECM, but it includes the influence of binding, thereby reducing the diffusivity. An alternative would be a more advanced study where arteries are decellularized and retested. This scenario is nonphysiologic; when this data is combined with the cellularized experimental data and modeled on the microstructural level the true diffusion of the molecule, and the influence of the arterial ultrastructure, could be better understood (3,12).

In addition, we report the differences in transport based on location for control (healthy) animals. In actuality, the diseased artery undergoes vascular remodeling during the development of disease and after intervention. Simultaneous, the deposition of lipids and calcium deposits can further change properties (57,58). This can be especially relevant because the dye will preferentially bind to lipids in the wall. The data in this manuscript is motivation to evaluate the properties based on location further, and provides a control situation to investigate location dependence in disease animal models.

A further limitation of this study was in the regression of data: a finite element model was built assuming homogenous dimensions in the circumferential data as averaged from histological sections. In reality, the vessel is heterogeneous in thickness and radius. Past studies have been implemented where non-homogeneity was investigated; however, experimental input would be required in our study to include this (3,4).

Our removal of the adventitia could be affecting total transport in our study. Elimination of the adventitia was unavoidable in our study because of the use of multiphoton microscopy. Multiphoton microscopy provides a method to determine concentrations on fully hydrated samples at different time points on the same sample. And while multiphoton microscopy can obtain greater depths than traditional confocal microscopy we were unable to achieve imaging depths greater than 300 μm. Our typical tissue thickness was 0.26 mm. Given that smooth muscle cells are the primary target for pharmaceuticals on drug-eluting stents and the advantages of nonlinear microscopy to track species movement, we felt the removal of the adventitia was valid.

While we show there are differences in species transport based on arterial region, there could be alternative underlying causes to restenosis. For instance, the hemodynamic and mechanical environments have been shown to change based on location (20,59). In an angioplasty scenario, restenosis can be a result of increased vascular stress or growth factor delivered remodeling (via diffusion or convection). Angioplasty has shown differences based on location with RC arteries maintaining better clinical success (60,61). The enhanced transport of growth molecules has been hypothesized to be partially responsible for the location differences regardless of the transport of drugs (15,62). Regarding drug-eluting stents, RC arteries maintain better clinical success in some studies (63). In the results presented in this manuscript the RC arteries had higher convection coefficients than the LADC arteries. This could indicate that convective transport could be more important to ensure drugs reach target areas at the proper times, given the clinical success. It addition, it was shown previously that given constant transport properties, drug delivery and retention can be changed dramatically by changing just the eluting profile from the stent. As such, non-optimized elution could also be responsible for late stage (non-thrombotic) stent restenosis (64). The location could be an influence on trends observed in restenosis, however multiple biochemical and biomechanical effects working in synergy are likely to be ultimately responsible.

In our study we reported how diffusive and convective-diffusive transport varies between coronary arteries and

their arterial length. While location may not be causative, the awareness of how transport varies could be important in any scenario where hydrophobic biomolecules are being delivered. We performed this via the use of nonlinear microscopy with image processing steps to obtain interstitial concentrations. Demonstration of the viability of a carbocyanine dye as a surrogate for drug-eluting stent drugs offers an inexpensive and relatively easy to implement alternative for researchers interested in investigating drug transport. The transport properties from this study are on similar animal subjects as previous work from our laboratory (20). This could be beneficial in the customized design of drug-elution optimized to the specific region. Stents could also utilize a differential coating along the length to best match to the properties reported here.

In addition, the Peclet number has been shown to be important in drug retention (4). Different classes of the sirolimus drug have differences in hydrophobicity, and therefore potentially different Peclet numbers (36). By this reasoning, the specific drug could be chosen based on the Peclet number for the particular location's transport properties since the convective and diffusive properties vary based on location. The diffusivity could be tuned by changing a chemical group on the sirolimus molecule to increase the hydrophobicity (36). This would, in theory, decrease the Peclet number. This could be used in a dual-drug scenario where the ends of the stent are coated with a different drug derivative of sirolimus than the center of the stent, given the clinical differences observed in the middle of the stent compared to the ends since the tissue at the ends could have different transport properties (21). These transport properties could also be broadly applied in that restenosis caused by growth factor deposition could be different based on arterial region. This could guide therapies were a paving approach is utilized in some locations to prevent prostenotic biomolecule transport (65). Combining mass transport and porohyperelastic properties from this study and previous reports of location dependence could be used in parametric finite element models of stent-based drug delivery to determine efficacy in drug delivery in coronary artery walls.

CONCLUSIONS

Our study demonstrates that the convective and diffusive transport of lipophilic molecules changes between the LADC and the RC arteries as well as along their length. These results may have important implications in optimizing drug delivery for the treatment of coronary artery disease.

ACKNOWLEDGMENTS AND DISCLOSURES

The authors would like to thank the University of Arizona Food Products and Safety Laboratory for help in sample acquisition. We would also like to thank Erica Pursell for help with histology work and Dr. Timothy Secomb and Dr. Urs Utzinger for their important scientific insight. The Advanced Intravital Microscope was funded through a NIH/NCRR 1S10RR023737-01. This work was supported, in parts, by an American Heart Association (AHA) Predoctoral Fellowship (11PRE7730024 to JTK), Achievement Rewards for College Scientists (ARCS; Mary Ann White Memorial Scholarship to JTK), and an AHA Grant-in-Aid (10GRNT4580045 to JPVG).

REFERENCES

1. Balakrishnan B, Dooley JF, Kopia G, Edelman ER. Intravascular drug release kinetics dictate arterial drug deposition, retention, and distribution. J Control Release. 2007;123:100–8.
2. Feenstraand PH, Taylor CA. Drug transport in artery walls: a sequential porohyperelastic-transport approach. Comput Methods Biomechanics Biomed Eng. 2009;12:263–76.
3. Hwangand CW, Edelman ER. Arterial ultrastructure influences transport of locally delivered drugs. Circ Res. 2002;90:826–32.
4. Hwang CW, Wu D, Edelman ER. Physiological transport forces govern drug distribution for stent-based delivery. Circulation. 2001;104:600–5.
5. Hwang CW, Wu D, Edelman ER. Impact of transport and drug properties on the local pharmacology of drug-eluting stents. Int J Cardiovasc Interv. 2003;5:7–12.
6. Kang SJ, Mintz GS, Park DW, Lee SW, Kim YH, Whan Lee C, *et al.* Mechanisms of in-stent restenosis after drug-eluting stent implantation: intravascular ultrasound analysis. Circ Cardiovasc Interv. 2011;4:9–14.
7. Levin AD, Vukmirovic N, Hwang CW, Edelman ER. Specific binding to intracellular proteins determines arterial transport properties for rapamycin and paclitaxel. Proc Natl Acad Sci U S A. 2004;101:9463–7.
8. Lovich MA, Creel C, Hong K, Hwang CW, Edelman ER. Carrier proteins determine local pharmacokinetics and arterial distribution of paclitaxel. J Pharm Sci. 2001;90:1324–35.
9. Yangand C, Burt HM. Drug-eluting stents: factors governing local pharmacokinetics. Adv Drug Deliv Rev. 2006;58:402–11.
10. Iwata A, Miura S, Mori K, Kawamura A, Nishikawa H, Saku K. Associations between metabolic factors and coronary plaque growth or arterial remodeling as assessed by intravascular ultrasound in patients with stable angina. Hypertens Res. 2008;31:1879–86.
11. Schafer K, Konstantinides SV. Update on the cardiovascular risk in obesity: endocrine and paracrine role of the adipose tissue. Hellenic J Cardiol. 2011;52:327–36.
12. Goriely AR, Baldwin AL, Secomb TW. Transient diffusion of albumin in aortic walls: effects of binding to medial elastin layers. Am J Physiol Heart Circ Physiol. 2007;292:H2195–201.
13. Brandl F, Kastner F, Gschwind RM, Blunk T, Tessmar J, Gopferich A. Hydrogel-based drug delivery systems: comparison of drug diffusivity and release kinetics. J Control Release. 2010;142:221–8.
14. Wan WK, Lovich MA, Hwang CW, Edelman ER. Measurement of drug distribution in vascular tissue using quantitative fluorescence microscopy. J Pharm Sci. 1999;88:822–9.

15. Consignyand PM, Miller KT. Drug delivery into the arterial wall: a time-course study with use of a lipophilic dye. J Vasc Interv Radiol. 1994;5:731–7.
16. Creel CJ, Lovich MA, Edelman ER. Arterial paclitaxel distribution and deposition. Circ Res. 2000;86:879–84.
17. Simon BR, Kaufmann MV, McAfee MA, Baldwin AL, Wilson LM. Identification and determination of material properties for porohyperelastic analysis of large arteries. J Biomech Eng. 1998;120:188–94.
18. Ayyalasomayajula A, Vande Geest JP, Simon BR. Porohyperelastic finite element modeling of abdominal aortic aneurysms. J Biomech Eng. 2010;132:104502.
19. Vande Geest JP, Simon BR, Rigby PH, Newberg TP. Coupled porohyperelastic mass transport (PHEXPT) finite element models for soft tissues using ABAQUS. J Biomech Eng. 2011;133:044502.
20. Keyes JT, Lockwood DR, Simon BR, Vande Geest JP. Deformationally dependent fluid transport properties of porcine coronary arteries based on location in the coronary vasculature. J Mech Behav Biomed Mater. 2012. doi:10.1016/j.jmbbm.2012.10.002.
21. Serruys PW, Degertekin M, Tanabe K, Russell ME, Guagliumi G, Webb J, *et al.* Vascular responses at proximal and distal edges of paclitaxel-eluting stents: serial intravascular ultrasound analysis from the TAXUS II trial. Circulation. 2004;109:627–33.
22. Ashby DT, Dangas G, Mehran R, Lansky AJ, Narasimaiah R, Iakovou I, *et al.* Comparison of clinical outcomes using stents *versus* no stents after percutaneous coronary intervention for proximal left anterior descending *versus* proximal right and left circumflex coronary arteries. Am J Cardiol. 2002;89:1162–6.
23. Cercek B, Sharifi B, Barath P, Bailey L, Forrester JS. Growth factors in pathogenesis of coronary arterial restenosis. Am J Cardiol. 1991;68:24C–33C.
24. Gibbonsand GH, Dzau VJ. The emerging concept of vascular remodeling. N Engl J Med. 1994;330:1431–8.
25. Daviesand MG, Hagen PO. Pathobiology of intimal hyperplasia. Br J Surg. 1994;81:1254–69.
26. Skwarek M, Grzybiak M, Kosinski A, Hreczecha J. Basic axes of human heart in correlation with heart mass and right ventricular wall thickness. Folia Morphol. 2006;65:385–9.
27. Crick SJ, Sheppard MN, Ho SY, Gebstein L, Anderson RH. Anatomy of the pig heart: comparisons with normal human cardiac structure. J Anat. 1998;193(Pt 1):105–19.
28. Caramori PR, Lima VC, Seidelin PH, Newton GE, Parker JD, Adelman AG. Long-term endothelial dysfunction after coronary artery stenting. J Am Coll Cardiol. 1999;34:1675–9.
29. Hofma SH, van der Giessen WJ, van Dalen BM, Lemos PA, McFadden EP, Sianos G, *et al.* Indication of long-term endothelial dysfunction after sirolimus-eluting stent implantation. Eur Hear J. 2006;27:166–70.
30. Molecular Probes, Inc. Product information: DiI derivatives for long-term cellular labeling. Invitrogen. 2005.
31. Food and Drug Administration. Summary of safety and effectiveness data. Drug-eluting coronary stent system (NIQ). Medtronic Vascular. 2008. http://www.accessdata.fda.gov/cdrh_docs/pdf6/P060033b.pdf.
32. Rashid F, Horobin RW, Williams MA. Predicting the behaviour and selectivity of fluorescent probes for lysosomes and related structures by means of structure-activity models. Histochem J. 1991;23:450–9.
33. Udipi K, Melder RJ, Chen M, Cheng P, Hezi-Yamit A, Sullivan C, *et al.* The next generation Endeavor Resolute Stent: role of the BioLinx Polymer System. EuroIntervention. 2007;3:137–9.
34. Kishore Udipi MC, Cheng P, Jiang K, Judd D, Caceres A, Melder RJ, Wilcox JN. Development of a novel biocompatible polymer system for extended drug release in a next-generation drug-eluting stent. J Biomed Mater Res A. 2007;85(7):7.
35. Gravier J, Navarro FP, Delmas T, Mittler F, Couffin AC, Vinet F, *et al.* Lipidots: competitive organic alternative to quantum dots for *in vivo* fluorescence imaging. J Biomed Opt. 2011;16:096013.
36. Burke SE, Kuntz RE, Schwartz LB. Zotarolimus (ABT-578) eluting stents. Adv Drug Deliv Rev. 2006;58:437–46.
37. Klausnerand RD, Wolf DE. Selectivity of fluorescent lipid analogues for lipid domains. Biochemistry. 1980;19:6199–203.
38. Graziani EI. Recent advances in the chemistry, biosynthesis and pharmacology of rapamycin analogs. Nat Prod Rep. 2009;26:602–9.
39. Chemical C. Product information item number 13346: rapamycin. Ann Arbor: Cayman Chemical; 2011.
40. Zhu W, Masaki T, Cheung AK, Kern SE. *In-vitro* release of rapamycin from a thermosensitive polymer for the inhibition of vascular smooth muscle cell proliferation. J Bioequiv Availab. 2009;1:3–12.
41. Karmakarand N, Lever MJ. Effects of high molecular weight solutes on fluid flux across the arterial wall. Hear Vessel. 1994;9:275–82.
42. Brugaletta S, Burzotta F, Sabate M. Zotarolimus for the treatment of coronary artery disease: pathophysiology, DES design, clinical evaluation and future perspective. Expert Opin Pharmacother. 2009;10:1047–58.
43. Li Y, Song Y, Zhao L, Gaidosh G, Laties AM, Wen R. Direct labeling and visualization of blood vessels with lipophilic carbocyanine dye DiI. Nat Protoc. 2008;3:1703–8.
44. Keyes JT, Borowicz SM, Rader JH, Utzinger U, Azhar M, Vande Geest JP. Design and demonstration of a microbiaxial optomechanical device for multiscale characterization of soft biological tissues with two-photon microscopy. Microsc Microanal. 2011;17:167–75.
45. Zoumi A, Lu X, Kassab GS, Tromberg BJ. Imaging coronary artery microstructure using second-harmonic and two-photon fluorescence microscopy. Biophys J. 2004;87:2778–86.
46. Delpy DT, Cope M, van der Zee P, Arridge S, Wray S, Wyatt J. Estimation of optical pathlength through tissue from direct time of flight measurement. Phys Med Biol. 1988;33:1433–42.
47. Vad S, Eskinazi A, Corbett T, McGloughlin T, Vande Geest JP. Determination of coefficient of friction for self-expanding stent-grafts. J Biomech Eng. 2010;132:121007.
48. Lovich MA, Philbrook M, Sawyer S, Weselcouch E, Edelman ER. Arterial heparin deposition: role of diffusion, convection, and extravascular space. Am J Physiol. 1998;275:H2236–42.
49. Borahand BJ, Yashonath S. Ions in water: role of attractive interactions in size dependent diffusivity maximum. J Chem Phys. 2010;133:114504.
50. Ho FG, Strieder W. A mean free path kinetic theory of void diffusion in a porous medium with surface diffusion. Asymptotic expansion in the Knudsen number. J Chem Phys. 1981;74:8.
51. Berezhkovskii AM, Dagdug L, Makhnovskii YA, Zitserman VY. Communications: Drift and diffusion in a tube of periodically varying diameter. Driving force induced intermittency. J Chem Phys. 2010;132:221104.
52. Dagdug L, Berezhkovskii AM, Makhnovskii YA, Zitserman VY. Particle size effect on diffusion in tubes with dead ends: nonmonotonic size dependence of effective diffusion constant. J Chem Phys. 2008;129:184706.
53. Ofir A, Dor S, Grinis L, Zaban A, Dittrich T, Bisquert J. Porosity dependence of electron percolation in nanoporous TiO2 layers. J Chem Phys. 2008;128:064703.
54. Harnek J, Zoucas E, Carlemalm E, Cwikiel W. Differences in endothelial injury after balloon angioplasty, insertion of balloon-expanded stents or release of self-expanding stents: an electron

microscopic experimental study. Cardiovasc Intervent Radiol. 1999;22:56–61.
55. Hillerand G, Weber K. Radioimmunoassay for tubulin: a quantitative comparison of the tubulin content of different established tissue culture cells and tissues. Cell. 1978;14:795–804.
56. Chambraud B, Radanyi C, Camonis JH, Shazand K, Rajkowski K, Baulieu EE. FAP48, a new protein that forms specific complexes with both immunophilins FKBP59 and FKBP12. Prevention by the immunosuppressant drugs FK506 and rapamycin. J Biol Chem. 1996;271:32923–9.
57. Loree HM, Kamm RD, Stringfellow RG, Lee RT. Effects of fibrous cap thickness on peak circumferential stress in model atherosclerotic vessels. Circ Res. 1992;71:850–8.
58. Lee RT, Grodzinsky AJ, Frank EH, Kamm RD, Schoen FJ. Structure-dependent dynamic mechanical behavior of fibrous caps from human atherosclerotic plaques. Circulation. 1991;83:1764–70.
59. Malek AM, Alper SL, Izumo S. Hemodynamic shear stress and its role in atherosclerosis. JAMA. 1999;282:2035–42.
60. Talley JD, Weintraub WS, Roubin GS, Douglas Jr JS, Anderson HV, Jones EL, *et al.* Failed elective percutaneous transluminal coronary angioplasty requiring coronary artery bypass surgery. In-hospital and late clinical outcome at 5 years. Circulation. 1990;82:1203–13.
61. Roubin GS, King 3rd SB, Douglas Jr JS. Restenosis after percutaneous transluminal coronary angioplasty: the Emory University Hospital experience. Am J Cardiol. 1987;60:39B–43B.
62. Slepian MJ, Gaballa MA. Vascular wall hydraulic conductivity increases following non-dissecting balloon stretch injury (abstract). Circulation. 1992;86:I-85.
63. Chen SL, Zhang JJ, Ye F, Liu ZZ, Zhu ZS, Lin S, *et al.* Crush stenting with drug-eluting stents: relevance of coronary bifurcation lesion location on angiographic and clinical outcomes. Clin Cardiol. 2010;33:E32–9.
64. Papafaklis MI, Chatzizisis YS, Naka KK, Giannoglou GD, Michalis LK. Drug-eluting stent restenosis: effect of drug type, release kinetics, hemodynamics and coating strategy. Pharmacol Ther. 2012;134:43–53.
65. Ashton JH, Mertz JA, Harper JL, Slepian MJ, Mills JL, McGrath DV, *et al.* Polymeric endoaortic paving: mechanical, thermoforming, and degradation properties of polycaprolactone/polyurethane blends for cardiovascular applications. Acta Biomater. 2011; 7:287–94.